Computers in Biology and Medicine 137 (2021) 104796

Contents lists available at ScienceDirect

Computers in Biology and Medicine

journal homepage: www.elsevier.com/locate/compbiomed

Analysis of the response of human iPSC-derived cardiomyocyte tissue to I_{CaL} block. A combined in vitro and in silico approach

Albert Dasí [a], Ismael Hernández-Romero [b], Juan F. Gomez [a,c], Andreu M. Climent [d], Jose M. Ferrero [a], Beatriz Trenor [a,*]

[a] Centro de Investigación e Innovación en Bioingeniería, Ci2B, Universitat Politècnica de València, Valencia, Spain
[b] Department of Signal Theory and Communications and Telematics Systems and Computing, Rey Juan Carlos University, Fuenlabrada, Spain
[c] Valencian International University, Valencia, Spain
[d] Instituto ITACA, Universitat Politècnica de València, Valencia, Spain

ARTICLE INFO

Keywords:
hiPSC-CM
hAdultV-CM
Re-entry
I_{CaL} block

ABSTRACT

The high incidence of cardiac arrythmias underlines the need for the assessment of pharmacological therapies. In this field of drug efficacy, as in the field of drug safety highlighted by the Comprehensive in Vitro Proarrhythmia Assay initiative, new pillars for research have become crucial: firstly, the integration of in-silico experiments, and secondly the evaluation of fully integrated biological systems, such as human induced pluripotent stem cell-derived cardiomyocytes (hiPSC-CMs). In this study, we therefore aimed to combine in-vitro experiments and in-silico simulations to evaluate the antiarrhythmic effect of L-type calcium current (I_{CaL}) block in hiPSC-CMs. For this, hiPSC-CM preparations were cultured and an equivalent virtual tissue was modeled. Re-entry patterns of electrical activation were induced and several biomarkers were obtained before and after I_{CaL} block. The virtual hiPSC-CM simulations were also reproduced using a tissue composed of adult ventricular cardiomyocytes (hAdultV-CMs). The analysis of phases, currents and safety factor for propagation showed an increased size of the re-entry core when I_{CaL} was blocked as a result of depressed cellular excitability. The bigger wavefront curvature yielded reductions of 12.2%, 6.9%, and 4.2% in the frequency of the re-entry for hiPSC-CM cultures, virtual hiPSC-CM, and hAdultV-CM tissues, respectively. Furthermore, I_{CaL} block led to a 47.8% shortening of the vulnerable window for re-entry in the virtual hiPSC-CM tissue and to re-entry vanishment in hAdultV-CM tissue. The consistent behavior between in-vitro and in-silico hiPSC-CMs and between in-silico hiPSC-CMs and hAdultV-CMs evidences that virtual hiPSC-CM tissues are suitable for assessing cardiac efficacy, as done in the present study through the analysis of I_{CaL} block.

1. Introduction

Cardiac arrhythmias are essentially electric disorders that cause mechanical dysfunction. As they are having an increasing impact on global mortality, now around 15–20% [1], the analysis of the electrical mechanisms involved in the genesis, and more importantly, the treatment, of arrhythmias is crucial.

Two promising methods have emerged in cardiac research: *in-vitro* experiments with stem cells and the use of *in-silico* theoretical models. The former has been broadly run since the discovery of human-induced Pluripotent Stem Cells (hiPSC) [2] and the well-established principle to differentiate them into cardiomyocytes (hiPSC-CMs). They encompass numerous medical applications, such as disease modeling [3], pharmacological assessment [4] and regenerative medicine [5]. Their effectiveness lies in their particular way of being generated, which allows them to retain the genomic composition of their source, enabling more accurate personalized medicine, such as the analysis of genetic alterations [6–9]. However, as their immaturity challenges their ability to reproduce the electrophysiological behavior of adult human ventricular CMs (hAdultV-CMs) and even to consider the results obtained as suitable, their use in cardiac research is still controversial. Among the major limitations, hiPSC-CMs present high electrophysiological variability, both compared to hAdultV-CMs and among different hiPSC-CMs cultures, incompletely developed Ca^{2+} cycling and slow propagation of the action potential (AP) [10]. The slow propagation, which results in low conduction velocity and cellular excitability, limits their use for

* Corresponding author.
E-mail address: btrenor@eln.upv.es (B. Trenor).

https://doi.org/10.1016/j.compbiomed.2021.104796
Received 7 March 2021; Received in revised form 2 August 2021; Accepted 22 August 2021
Available online 25 August 2021

studying arrhythmogenic mechanisms such as conduction abnormalities. In this sense, nowadays there is a global tendency to generate newer cellular maturation techniques and improve existing ones [11,12] to make hiPSC-CMs more reliable and comparable to hAdultV-CMs.

The use of *in-silico* models has promoted the formulation of several virtual hAdultV-CM [13] and even hiPSC-CM models [14–16]. Different *in-silico* studies comparing the hAdultV-CM and hiPSC-CM response to drugs have been performed. Some of these [14] have analyzed the similarities and differences of the respective computational models when both cellular types were subject to the effects of ion current block. Also, *in-vitro* experiments have assessed the legitimacy of using hiPSC-CMs for drug screening [17,18].

Therefore, the combination of experimental and computational studies emerges as a strong research tool for assessing the arrhythmogenic effects of specific drugs. Indeed, in disease modeling and pharmacological assessment, the unified *in-silico* and *in-vitro* approach has been presented as a solid alternative to overcome the current methodological limitations [14]. The transcendence of these techniques has been acknowledged by the pharmaceutical industry and considered as a reference in the *Comprehensive in Vitro Proarrhythmia Assay* (CiPA) initiative [19], a new concept of pharmacological assessment that emphasizes the support of *in-silico* models to better understand ionic mechanisms in *in-vitro* observations. *In-vitro* and *in-silico* models of hiPSC-CMs have been successfully used to study the arrhythmogenic phenotypes of a number of cardiac diseases, such as atrial fibrillation, hypertrophic cardiomyopathy and, predominantly, long QT syndrome [10]. Likewise, *in-vitro* and *in-silico* studies with hiPSC-CMs have been performed to assess the pro-arrhythmic risk and cardiotoxicity of numerous compounds. Following the lead of conducting simulations and experiments for safety assessment [19], the application of hiPSC-CMs for testing drug efficacy in joint research emerges as promising [10].

In this work, we combined *in-vitro* experiments and *in-silico* simulations to assess the antiarrhythmic efficacy of L-type calcium current (I_{CaL}) block in hiPSC-CM tissues. Through this study we aimed to demonstrate (1) the suitability of virtual hiPSC-CM tissues to replicate experimental phenomenon in higher dimensions (2D), using a unified *in-vitro/in-silico* approach, and (2) the high reliability of hiPSC-CM theoretical models in simulating the behavior of virtual hAdultV-CMs.

For this, we cultured hiPSC-CM suspensions and performed computer simulations with a virtual hiPSC-CM tissue. We studied the *in-vitro* and *in-silico* findings to understand the changes in re-entry dynamics before and after I_{CaL} block. Since Paci et al. [14] highlighted a higher sensitivity of the cellular hiPSC-CM model to I_{CaL} block compared to hAdultV-CM [13], we wondered whether the results obtained with the virtual hiPSC-CM tissue could be extrapolated to hAdultV-CM, and so replicated the simulations conducted with hiPSC-CM using a virtual hAdultV-CM tissue. The comparison between *in-silico* hiPSC-CM and hAdultV-CM strengthened the results obtained through the combined *in-vitro/in-silico* hiPSC-CM approach.

2. Materials and methods

2.1. In-vitro experiments

2.1.1. Cell cultures

In vitro experiments were performed following the protocol previously described [9]. Briefly, human pluripotent stem cells were seeded at a density of 125,000 cells/cm^2 in mTeSR (StemCell Technologies) for 48 h onto Matrigel-coated cell-culture dishes (BD Biosciences). Differentiation started by treating the cells with 12 μM CHIR99021 (Selleck) in RPMI (Invitrogen) supplemented with B27-insulin (Life Technologies), 2 mM L-glutamine, 0.1 mM 2-mercaptoethanol, nonessential amino acids and penicillin-streptomycin (RPMI/B27-insulin medium). On day 1, cells were washed with RPMI to remove the inhibitor, which was substituted to RPMI/B27-insulin on day 2. After 72 h, cell cultures were treated with 5 μM Wnt inhibitor IWP4 (Stemgent) in RPMI/B27-insulin medium. On day 5, RPMI was applied to wash cells and RPMI/B27 medium was changed every 48 h. By day fourteen, monolayers were spontaneously beating and the experiments were performed three days after.

2.1.2. Optical mapping system

Electrophysiological analysis was performed following the protocol described in [9]. Di-4-ANBDQPQ (donated by Dr. Loew, University of Connecticut Health Center, USA) and Rhod-2(AM) (Ca^{2+} sensitive probe, TEFLabs, Inc, Austin, TX. USA) were loaded in the cells to record voltage and calcium imaging.

2.1.3. Dye loading

Calcium imaging was performed by staining hiPSC-CMs during 30 min under incubation condition with a 3 mL of a modified Krebs solution at 36.5 °C (containing, in mM: NaCl, 120; NaHCO3 25; $CaCl_2$ 1.8; KCl 5.4; $MgCl_2$ 1; glucose 5.5; H_2O_4PNa H_2O 1.2) with Rhod-2 AM dissolved in DMSO (1 mM stock solution; 3.3 μl per ml in culture medium) and Probenecid (TEFLabs, Inc, Austin, TX, USA) at 420 μM. For voltage imaging, culture media was changed to fresh Krebs with di-4-ANBDQPQ voltage dye dissolved in pure ethanol (27.3 mM stock solution, 2 μl per ml in culture medium) and Pluronic F-127 (Life Technologies) to a final concentration of 0.2–0.5%.

Voltage dye was incubated during 5 min. Finally, medium was changed to fresh Krebs solution at 36.5 C supplemented with 10 μM blebbistatin to avoid movement. Chemicals were obtained from Sigma-Aldrich (Dorset, UK) and Fisher Scientific Inc. (New Jersey, USA).

2.1.4. Experimental protocol and imaging processing

Cell cultures were spontaneously beating prior to the external stimulation. A gradual pacing protocol was applied at increasing rates, starting with a pacing cycle length (CL) of 1000 ms (ms) and increasing the frequency until the onset of fibrillation. Stimulation was performed by using custom made pacing system and using platinum-iridium catheters. Amplitude of stimulation was selected individually for each cell culture as the minimum power that achieved local pacing. Optical mapping recordings were acquired under basal conditions and after the administration of verapamil (4 μM in Krebs solution, Sigma-Aldrich, Dorset, UK) in 6 monolayers at 36.5 °C. Cultures were analyzed with the optical mapping technique. For each sample, two optical mapping movies were recorded, one during control conditions and a second one after the administration of verapamil. The concentration of 4 μM was selected to maximize the calcium blocker effect of verapamil but limiting the potassium blocker properties of this drug [20]. Optical mapping signals were analyzed using our customized software designed in MATLAB. Raw data was filtered applying a spatial Gaussian filter (size 7×7 pixels) and a temporal Savitzky-Golay filter (size 15 samples). For each pixel, baseline was removed by subtracting the lower envelope of the signals. Finally, voltage and calcium signals of each pixel were normalized between 0 and 1.

2.1.5. Rotor and dominant frequency identification

Rotor localization was automated based on identification of singularity points (SPs) in the phase signal map obtained with the Hilbert transform [21]. SPs were defined as the points in the phase map surrounded by phases from $-\pi$ to π. SPs were considered as rotors if the re-entry was present in the tissue for the duration of at least one full rotation.

For dominant frequency analysis, the power spectral density of all signals was computed using a periodogram (2s Hamming window, 50% overlap, sampling rate 500 Hz). The highest peak was selected as the dominant frequency and harmonics discarded [22].

2.1.6. Statistical analysis

For each monolayer, both control and verapamil electrophysiological properties were compared by using paired student's t-test. Results

were considered significant for p-values lower than 0.05.

2.2. In-silico simulations

In-vitro experiments performed on hiPSC-CM cultures were replicated *in-silico* using a virtual 2D tissue. The Paci et al. [15] model was adopted to reproduce the hiPSC-CM AP. The results obtained with virtual hiPSC-CMs were compared against an equivalent *in-silico* tissue composed of hAdultV-CMs. A modified version of the O'Hara et al. [13] model as in Mora et al. [23] was implemented for the latter. Material and geometrical properties, such as the level of anisotropy, conduction velocity (CV) and the size and shape of the tissues were defined on the basis of experimental data [9,24] (See Supporting *Information*– Table S1 for details).

In both tissues, two different scenarios were analyzed: one defined as control, with no changes in I_{CaL} formulation, and another established as I_{CaL} block, where the maximum conductance of I_{CaL} was decreased by 70% [9] in order to simulate the effects of the drug administration. To assess whether our results were dose-dependent, additional degrees of current blockade were studied (the results are given in the Supporting Information – Degree of current blockade. Figure S2 and S3). Similarly, the effects of I_{CaL} block were compared against a situation in which verapamil perfusion was modeled in-silico. For the latter, both the rapid rectifier potassium current (I_{Kr}) and I_{CaL} were blocked. A detailed comparison between control, I_{CaL} block and verapamil effect can be found in the Supporting Information. Computational simulations were performed using ELVIRA [25] (see Supporting Information for details), developed in FORTRAN 90 programming environment (The IBM Mathematical Formula Translating System).

2.2.1. Vulnerable window for re-entry

Re-entry induction was achieved by applying a standard S1–S2 cross-shock protocol (explained in detail in the Supporting Information-Figure S1). The vulnerable window (VW) for re-entry was defined as the time interval within which the application of an S2 stimulus led to a re-entry pattern. Other biomarkers, such as the core and frequency of the re-entry ($f_{reentry}$), wavelength, and cellular excitability, were evaluated once sustained re-entries (>3 s) were established. A phase analysis was conducted to track the rotor tip movement through phase SPs, as in previous works [26–28].

2.2.2. Frequency of the re-entry

The excitation frequency was determined for every node of the tissue as the inverse of the average CL. The $f_{reentry}$ was subsequently computed as the mean of the individual frequencies. A statistical analysis of the $f_{reentry}$ was undertaken (0.01 level of significance) considering the individual frequency in each node. Since each tissue was composed by 251.001 nodes, extremely large samples defined each situation –control and I_{CaL} block–. Accordingly, the 95% confidence interval (CI) was reported, for the sake of reliability regardless of the size of the sample [29].

2.2.3. Trajectory of the rotor tip and zone of block

The wavelength of the re-entry was estimated through the trajectory of the rotor tip (SPs). A detailed analysis of the wavefront propagation was conducted in the first re-entry loop for control and drug conditions. The zone of block (ZoB) was defined as the region of the virtual tissues where the electrical propagation was blocked and the AP extinguished. Two approaches were followed to characterize the ZoB. In the first approach, the ZoB was determined by studying the main currents responsible for cellular depolarization (i.e., the fast sodium current (I_{Na}) and I_{CaL}). These inward currents were chosen as several authors [30,31] have asserted their importance for re-entry maintenance while challenging the role of the potassium currents. Thus, the time course of I_{Na} and I_{CaL} were evaluated locally, in the specific nodes of the tissue where the AP failed to propagate. A global analysis, comprising every node of the tissue was also conducted. Normalized current maps were built for I_{Na}, I_{CaL} and the contribution of $I_{CaL} + I_{Na}$ during the first re-entry loop. For the sake of comparison in control and I_{CaL} block, normalization was achieved with respect to the maximum peak current in control and drug conditions. The ZoB was defined in the normalized maps using the inward current of the SPs as reference thresholds. Five thresholds were computed: the minimum value for $I_{CaL} + I_{Na}$ of the rotor tip points (SPs), the mean value minus the standard deviation, the mean value, the mean value plus the standard deviation and the maximum value for $I_{CaL} + I_{Na}$ of the SPs points.

The second approach adopted to characterize the ZoB considered every current involved in the AP development. For this the safety factor (SF) was computed using the formulation from Romero et al. [32]. Several studies have highlighted the effectiveness of the SF in quantifying and interpreting propagation block [32–36], which helps determine the minimum requirements for uninterrupted propagation [33]. The comparison of the ZoB resulting from the normalized current maps (first approach) and the one from the SF analysis (second approach) was crucial to highlight the important role of depressed cellular excitability in re-entry dynamics.

3. Results

3.1. In vitro re-entries

To confirm verapamil's antiarrhythmic properties and to test its effects on the re-entry dynamics, re-entries were generated and analyzed in hiPSC-CM cultures before and after drug administration.

Fig. 1 displays representative activity (upper row in panels A and B) and phase maps (lower row in panels A and B) of a representative in-vitro episode. In this example, a counterclockwise re-entry can be seen in different snapshots during control conditions and verapamil administration. During the control conditions (panel A), the meandering was stable and remained attached to the same region. In this group, the anchoring areas of re-entry, represented by SPs in light blue in the lower row of panel A, circumscribed a perimeter of 0.07 ± 0.02 cm and the dominant frequency was 2.48 ± 0.16 Hz. In contrast, the acquired SPs shown in light blue in the lower row of panel B, were scattered over a larger area increasing the meandering after verapamil perfusion. In these cases, the observed perimeter rose to 0.20 ± 0.05 cm and the dominant frequency was reduced to 2.21 ± 0.07 Hz.

3.2. In silico re-entries

Similar to the experimental observations, blocking I_{CaL} increased wavefront meandering in the virtual hiPSC-CM tissue. The rotor tip (SPs), which remained anchored in a small region during control conditions, described an irregular and unstable circuit after I_{CaL} block (perimeter of 0.12 cm for control conditions vs. 1.2 cm after I_{CaL} block) (Fig. 2A). Identical re-entry dynamics were exhibited in the virtual hiPSC-CM tissue after single I_{CaL} and combined $I_{CaL} + I_{Kr}$ block (see Supporting Information – Figure S4). Similarly, blocking I_{CaL} prompted wavefront meandering in the virtual hAdultV-CM tissue (perimeter of 4.84 cm in control vs. 22.64 cm after I_{CaL} block) (Fig. 2B), although the anisotropic properties of hAdultV-CMs made the re-entry dynamics differ slightly from those of the virtual hiPSC-CM tissue.

3.2.1. Frequency of the re-entry

I_{CaL} block led to wavefront meandering and heterogeneous cell depolarization. These heterogeneities were exacerbated after each re-entry loop as the wavefront meandering was irregular. The more irregular the circuit described by the rotor tip, the increasing CL differences from beat to beat. Together with the sharp rise of the wavelength observed after blocking I_{CaL}, CL heterogeneities prompted a reduction of the $f_{reentry}$ of 6.9% (from 1.623 [1.622, 1.624] Hz to 1.511 [1.510, 1.512] Hz (mean [CI]); $p < 0.01$) and 4.2% (from 3.872 [3.871, 3.873] Hz to 3.709 [3.707

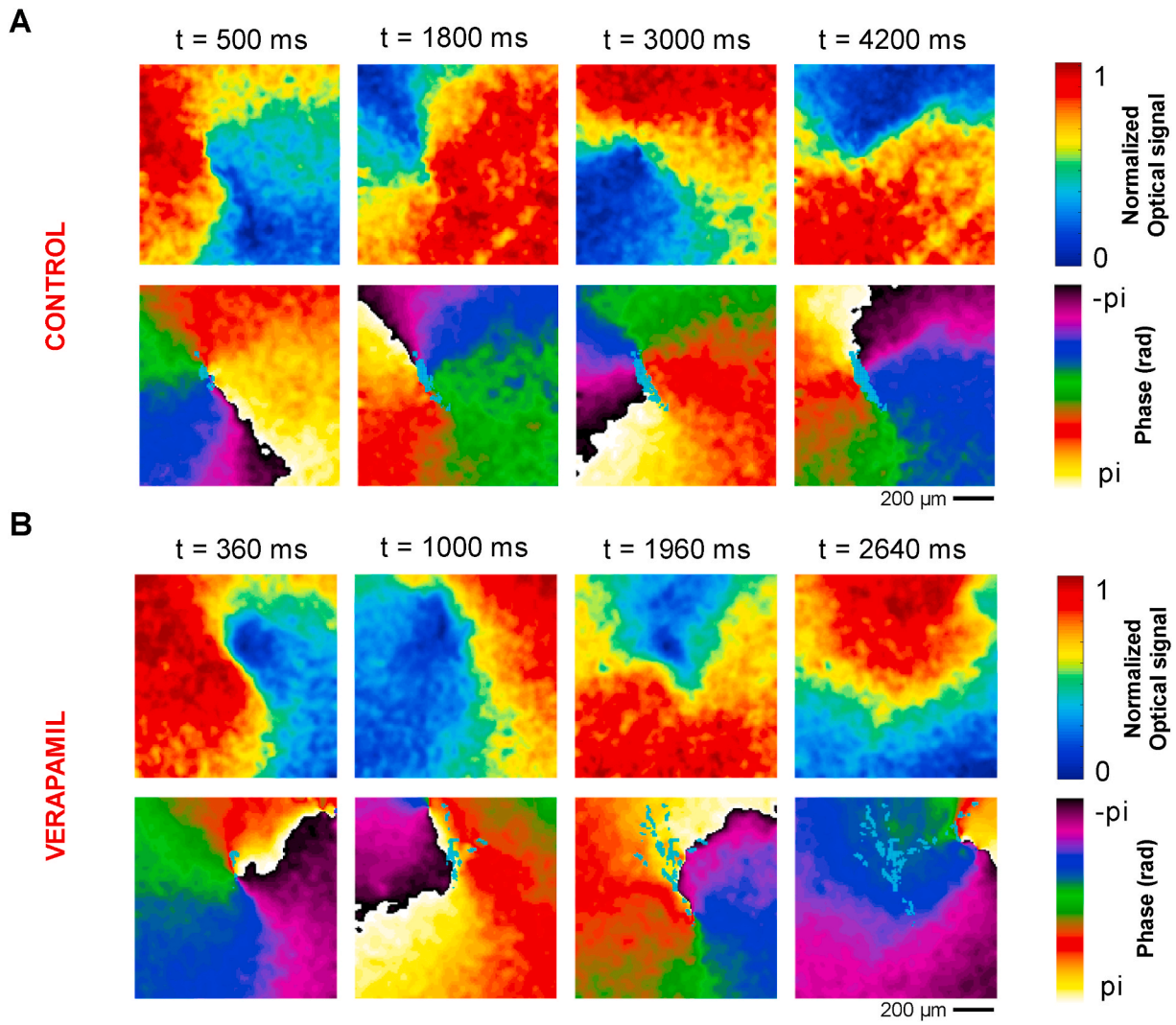

Fig. 1. Effects of verapamil administration on re-entry dynamics. Normalized optical signals and phase maps snapshots at different instants of time during basal conditions (panel A) and after administration of verapamil (panel B). The rotor tip movement is represented by the light blue points in the phase maps. The time instants above each snapshot indicate the elapsed time after the onset of the re-entry.

3.712] Hz (mean [CI]); $p < 0.01$) in the hiPSC-CM and hAdultV-CM tissues, respectively (Fig. 3B).

Fig. 3 illustrates the agreement between experimental observations and computer simulations. In both cases, the increased wavelength of the re-entry after drug perfusion/modeling reduced the activation rate in hiPSC-CM cultures/tissue. A more moderate reduction was observed in the virtual hAdultV-CM tissue.

3.2.2. *Vulnerable window for re-entry in virtual tissues*

The VW was reduced by 48.25% (from 114 ms to 59 ms) in the virtual hiPSC-CM tissue after I_{CaL} block, implying a lower probability of re-entry induction. Further degrees of VW shortening were observed when more severe I_{CaL} block was evaluated (see Supporting information – Fig. S6). No proper comparison of the VW could be made in the virtual hAdultV-CM tissue, since no sustained re-entries (>3 s) were observed after blocking I_{CaL}. The longest re-entry was self-terminated after 1100 ms. However, most of them vanished after a few re-entry loops (<1 s), due to excessive wavefront meandering. Sustained re-entries were found in the virtual hiPSC-CM tissue when I_{CaL} was blocked by 70%, but not after a 90% block, which also promoted the vanishing of the re-entry (see Supporting Information). Under control conditions, re-entries were sustained (>3 s) in both virtual tissues.

3.2.3. *Mechanistic investigation of I_{CaL} block*

To understand the effects of I_{CaL} block on re-entry dynamics, a mechanistic investigation was performed following the two approaches described in the methods section. Focusing only on inward currents in the first approach, both the local and global analysis highlighted the importance of I_{CaL} for AP generation and propagation. The local analysis, which assessed cellular availability through the evaluation of I_{CaL} and I_{Na} in specific nodes of the tissue, was conducted only on the virtual hiPSC-CM tissue. The anisotropic properties of hAdultV-CM increased the complexity of re-entries, hampering the comparison between control and I_{CaL} block situations. The hiPSC-CM tissue, however, exhibited comparable scenarios in terms of wavefront location and dynamics after a few re-entry loops (Fig. 4A - First Column).

Fig. 4 illustrates the cellular mechanisms underlying the increased meandering after I_{CaL} block compared to the control situation. The locations of the yellow node (drug situation) and blue node (control situation) were chosen so that in both situations both nodes were under the same propagation conditions and yet conduction succeeded in the blue node (control situation) and failed in the yellow (drug situation). To determine why the AP vanished under I_{CaL} block and not in control despite presenting similar initial conditions, a second node (green node) of the tissue in which I_{CaL} had been blocked was analyzed. The comparison of the ionic traces of the yellow and green nodes revealed that

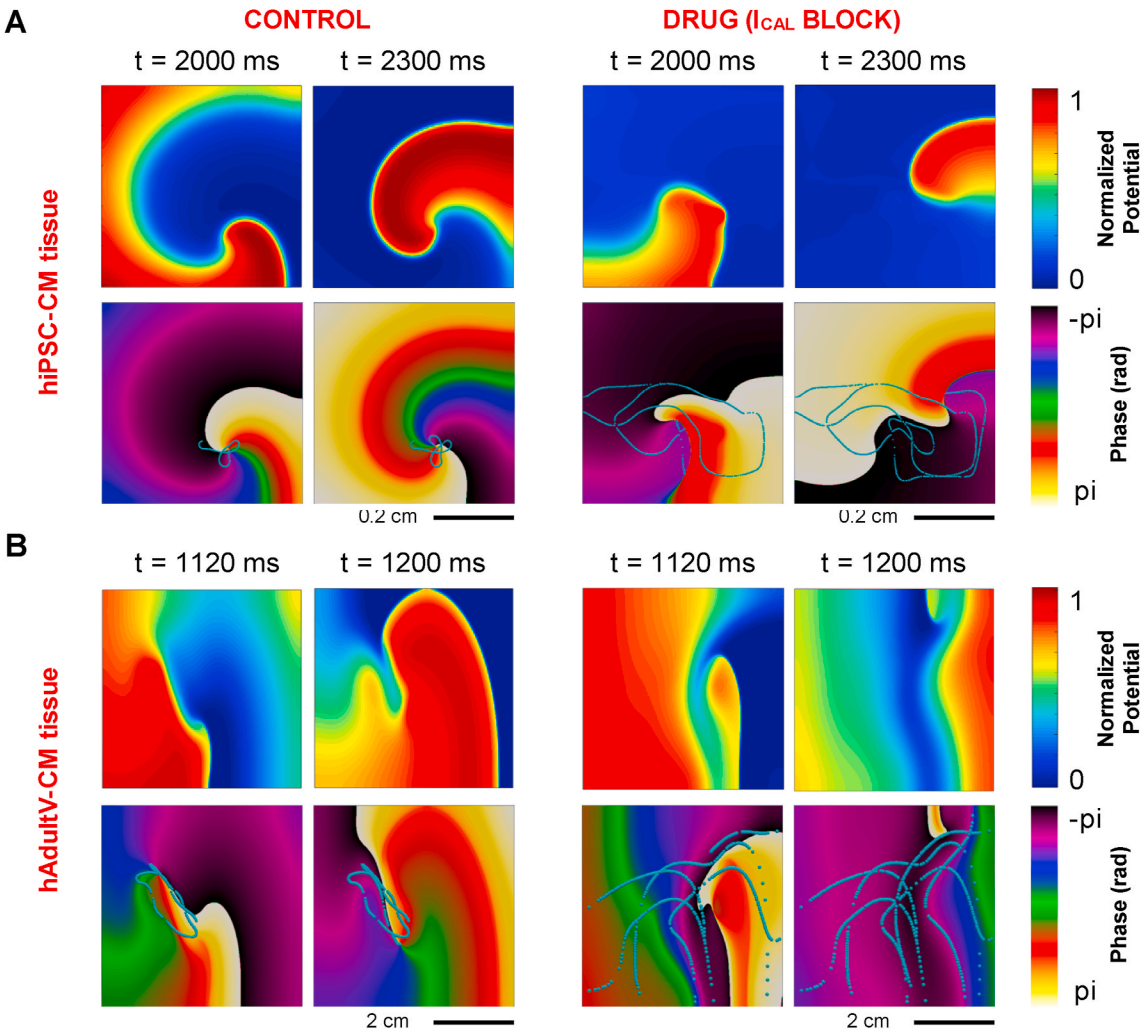

Fig. 2. Snapshots of the transmembrane voltage (potential) and phase maps at different time steps for the virtual hiPSC-CM (panel A) and hAdultV-CM (panel B) tissues. The rotor tip movement is represented by the dotted blue line in the phase maps. The time steps above each snapshot indicate the elapsed time after the S1 stimulus.

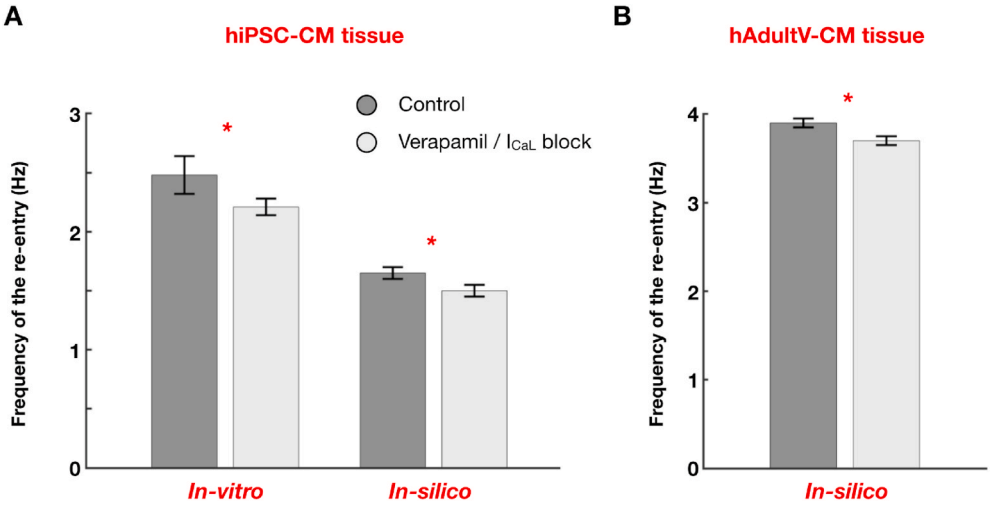

Fig. 3. Frequency of the re-entry (mean ± standard deviation) measured in A) hiPSC-CM cultures/tissues and B) virtual hAdultV-CM tissues. * denotes a level of significance below 0.05.

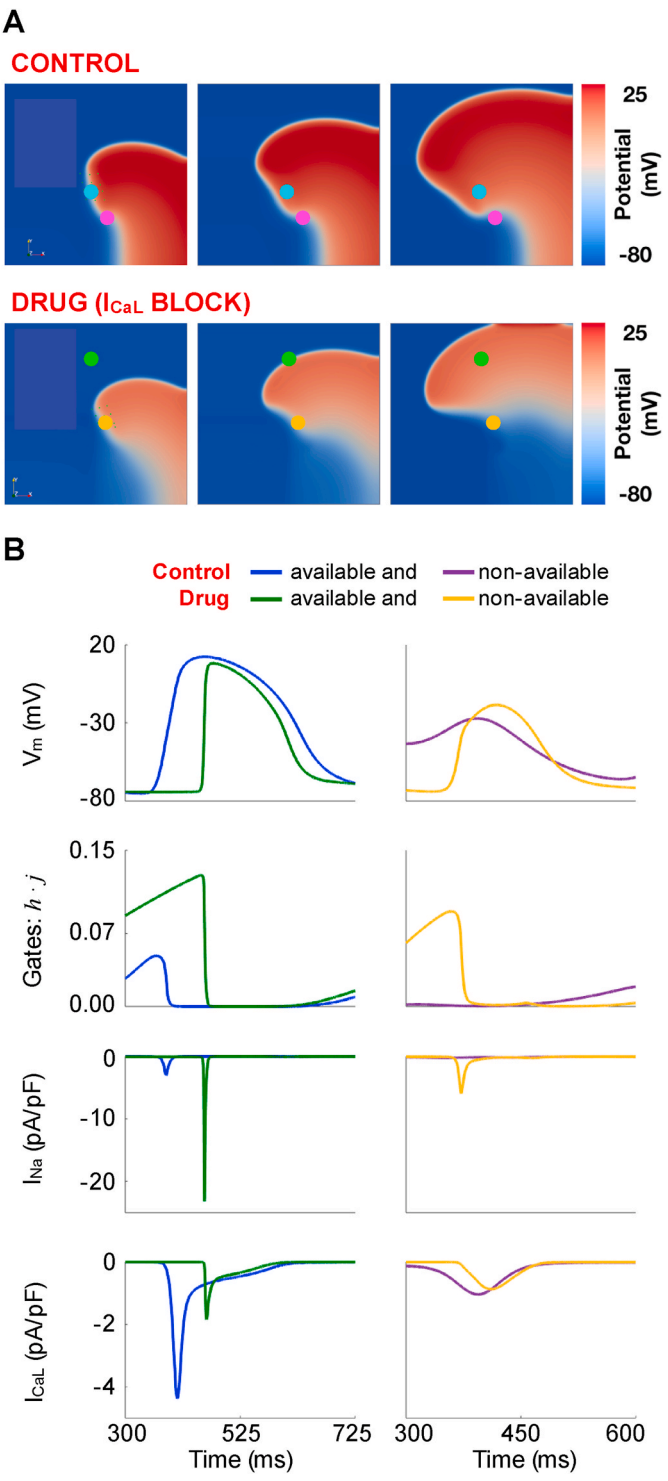

Fig. 4. Local analysis of cellular availability in the virtual hiPSC-CM tissue. A) Location of the analyzed nodes in panel B in control and drug conditions. B) Time course of the transmembrane voltage (V_m), fast sodium current (I_{Na}), L-type calcium current (I_{CaL}) and the product of sodium inactivation gates "h" and "j"(h · j) of the indicated nodes in panel A. Blue and green curves refer to the nodes where the propagation succeeded in control and drug tissue, respectively. Purple and yellow curves refer to the nodes where the wavefront was extinguished.

depressing I_{CaL} made the AP depolarization strongly dependent on I_{Na}, so that only the cells with a high I_{Na} amplitude were able to generate and propagate the AP.

In terms of re-entry dynamics, blocking I_{CaL} favored wavefront meandering as follows: After a complete re-entry loop, the wavefront reached the cells that had recently been depolarized. Since these cells had little time to recover from the previous activation, the product of the "h" and "j" (h · j) sodium inactivation gates was considerably depressed (Fig. 4B – green vs. yellow curves). In control conditions, the great contribution of I_{CaL} during the second phase of the AP allowed AP generation and propagation in spite of a reduced "h·j" (see blue curves in Fig. 4). In contrast, when I_{CaL} was blocked, the reduced availability of sodium inactivation gates and the reduced calcium expression led to AP extinction (see yellow curves in Fig. 4B).

The lower cellular availability resulting from blocking I_{CaL} was also observed in both virtual tissues through the global analysis of the inward currents (Fig. 5). The block of I_{CaL} (Fig. 5 – I_{CaL}) favored a global rise in I_{Na} compared to the control situation (Fig. 5– I_{Na}), as predicted in Fig. 4 and Figure S3, which was still insufficient to overcome the huge reduction of I_{CaL} (Fig. 5 – I_{CaL} + I_{Na}). Although the role of I_{Na} in the control tissue was less than under drug conditions, the important role of I_{CaL} during cellular depolarization meant that globally, the generation and propagation of the AP was more likely under control conditions, when both currents were acting. The computation of the ZoB revealed that the privation of I_{CaL} yielded to bigger re-entry cores (i.e., bigger ZoB) in both virtual hiPSC-CM and hAdultV-CM tissues (Fig. 5 – ZoB). Repeating the simulations with combined I_{CaL} + I_{Kr} block in the virtual hiPSC-CM tissue produced similar ZoB to that found when only I_{CaL} was blocked (see Supporting Information – Figure S5).

3.2.4. *Source-sink relationship*

The second approach was based on the SF, which encompasses all the currents involved in the generation of the AP as well as the passive properties of the tissue. Fig. 6 shows the distribution of the SF across both virtual tissues in control and under drug effects. According to the formal definition of the SF, values lower than one correspond to propagation block, so that the ZoB in Fig. 6 is shown as the regions in which the SF is lower than one (dark blue). These zones were bigger after I_{CaL} block (right column) in both virtual tissues. Interestingly, the ZoB obtained through the normalized maps and the SF (i.e., considering only the inward currents vs. all currents in the AP model) were very similar, which proves the leading role of the inward current in sustained propagation.

4. Discussion

The present study was conducted to determine the behavior of a hiPSC-CM culture/tissue when cells were subject to I_{CaL} block in a combined in-vitro/in-silico approach. As its specific aim was to analyze re-entry dynamics and the arrhythmogenic properties of blocking I_{CaL} using hiPSC-CMs, it revealed not only the promising potential of combining experimental observations with computational simulations but also the suitability of hiPSC-CMs for pharmacological assessment and generally in cardiac research. Its main findings are as follows: (i) I_{CaL} block promotes the meandering of the wavefront in the following scenarios: in-vitro hiPSC-CM culture and in-silico hiPSC-CM and hAdultV-CM tissues; (ii) likewise, in these scenarios $f_{reentry}$ was reduced in the presence of I_{CaL} block in a similar proportion; (iii) specific dynamic aspects of the re-entrant circuits remained different in the virtual hiPSC-CM and hAdultV-CM tissues. However, the major mechanisms were similar, so that, (iv) blocking I_{CaL} hampers re-entry induction and maintenance in experimental hiPSC-CM cultures and in virtual hiPSC-CM and hAdultV-CM tissues. Overall, this study highlights the suitability of virtual hiPSC-CM tissues to capture the dynamics of experimental hiPSC-CM cultures and their similar behavior to hAdultV-CMs.

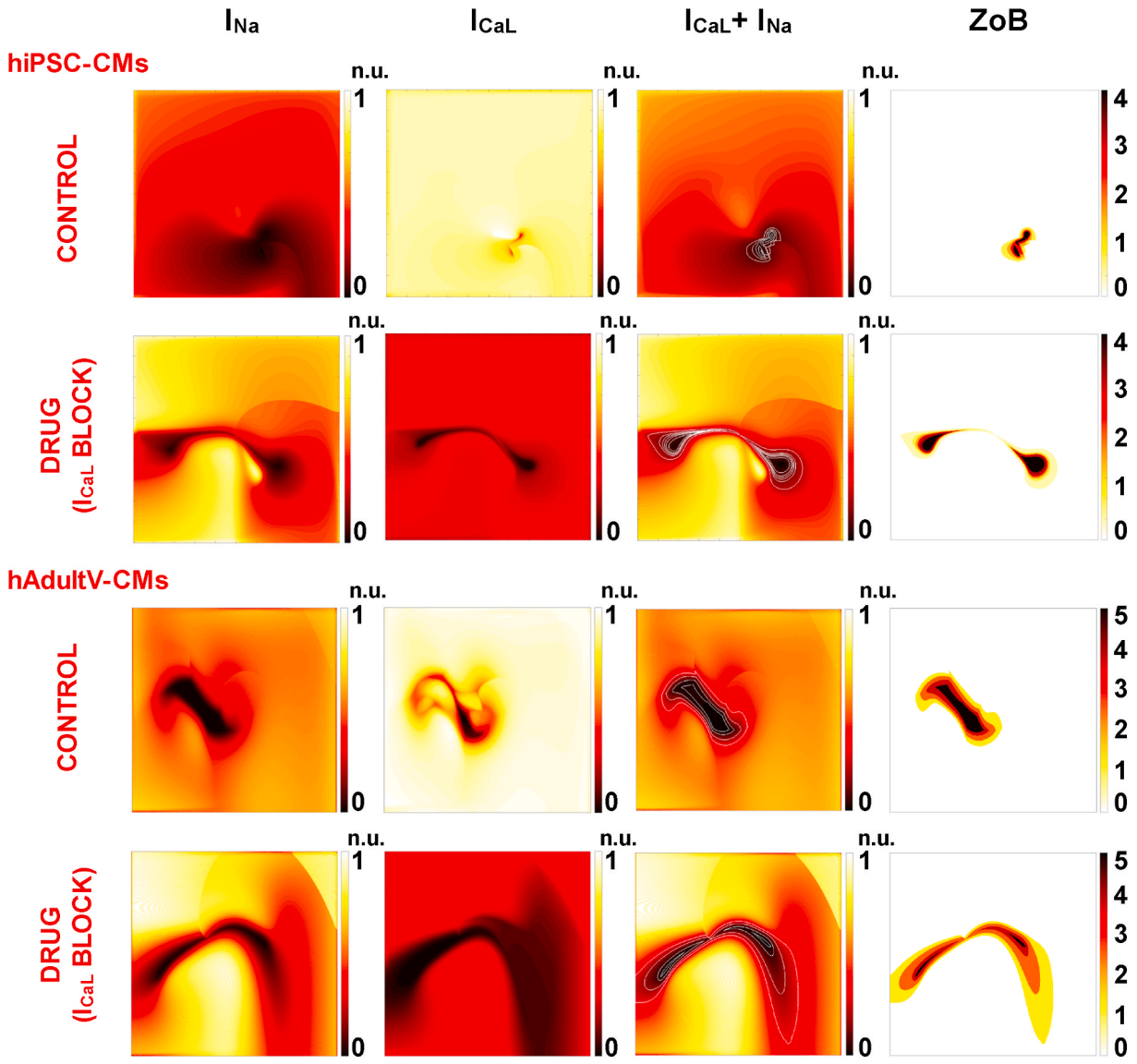

Fig. 5. Normalized maps (n.u.) of ion currents in the first re-entry loop and zone of block (ZoB) in virtual hiPSC-CM tissue and virtual hAdultV-CM tissue. First column: normalized peak of the fast sodium current (I_{Na}), second column: normalized peak of L-type calcium current (I_{CaL}), third column: normalized peak sums of I_{Na} and I_{CaL}. The normalization was performed in each section, I_{Na}, I_{CaL} and $I_{CaL} + I_{Na}$. The fourth column illustrates the zone where the wavefront is blocked, ZoB, according to 5 thresholds: the minimum value for $I_{CaL} + I_{Na}$ the rotor tip points (value 1), the mean value minus the standard deviation (value 2), the mean value (value 3), the mean value plus the standard deviation (value 4) and the maximum value (value 5).

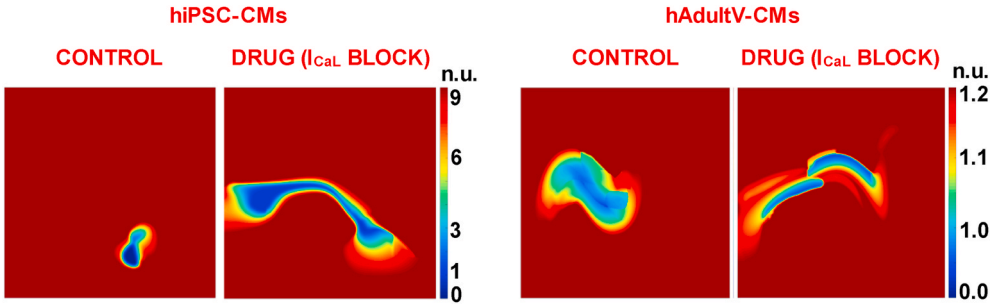

Fig. 6. Activation sequence and distribution of the safety factor (SF) in control and I_{CaL} block for hiPSC-CM and hAdultV-CM tissues.

4.1. Use of in-silico hiPSC-CM vs. hAdultV-CM tissues

A large body of cardiac experimental research relies on in-vitro hiPSC-CM cultures. Yet, when combined in-vitro/in-silico studies are performed, the results obtained in hiPSC-CM cultures are usually replicated and analyzed using theoretical hAdultV-CM cellular or tissue models [19]. In the present study, we emphasize the suitability of using hiPSC-CM computational models to consolidate and understand

observations obtained from in-vitro experiments with hiPSC-CMs. Conducting the same simulations in virtual hAdultV-CM and hiPSC-CM tissues was crucial to show that the latter faithfully reproduces the electrophysiological behavior of theoretical hAdultV-CMs models.

Although the cellular models for hiPSC-CM and hAdultV-CM differ in their formulation (regarding absolute and relative amplitudes and the number and type of currents), the results obtained showed that both models respond similarly to I_{CaL} block, at least in 2D simulations. This is especially interesting, considering the fact that the hiPSC-CM AP model is much more sensitive to I_{CaL} variations than the hAdultV-CM AP model, as reported by Paci et al. [14]. Indeed, the electrophysiological differences exhibited between hiPSC-CMs and hAdultV-CMs [10] prompted the development of computational tools capable of extrapolating the results obtained with hiPSC-CMs to hAdultV-CMs. Physiological metrics and statistical models [46] have been developed in a single-cell environment to predict the response of both cellular types to the effects of drugs. However, the application of these tools to higher dimensional levels urges re-evaluation. Studies [14,46] comparing the response to I_{CaL} block in single cell have reported a mismatch between hiPSC-CMs and hAdultV-CMs. However, in this study we have observed similar responses in 2D virtual tissues. Therefore, the results obtained in single cells may not necessarily match those of tissue or organ level. The development of tools for bridging the gap between hiPSC-CMs and hAdultV-CM in higher dimensional levels, therefore, remains very much needed.

Although similar mechanisms were observed between hiPSC-CMs and hAdultV-CMs, specific differences in the re-entry dynamics arose. This was mainly attributed to the anisotropic degree and the higher CV in the virtual hAdultV-CM vs. hiPSC-CM tissues. First, as CV was higher in the virtual hAdultV-CM tissue, more space was required to induce sustained re-entries. Together with the imposed degree of anisotropy, which favored AP conduction in the longitudinal over the transversal direction, the baseline re-entry core was much bigger in the hAdultV-CM than in the hiPSC-CM tissue. As the substantial size of the core in the former reduced the space in which the wavefront could move freely, when I_{CaL} was blocked and meandering considerably increased, the available space became so limited that re-entries were self-terminated after completing a few loops. However, re-entry also vanished after a 90% block of I_{CaL} in the hiPSC-CM tissue (see Supplemental Material).

An in-depth investigation [47] into re-entry dynamics showed a pivotal role of anisotropy on wavefront curvature, both in control and after pharmacological treatment. Thus, the anisotropy considered in the virtual hAdultV-CM tissue simulations is in part responsible for the differences in the re-entry dynamics with respect to the hiPSC-CMs isotropic tissue. If the same diffusion coefficient and degree of anisotropy were considered in both tissues, the reentry patterns would present many more similarities. In this sense, achieving similar conduction properties in hiPSC-CM cultures to that in hAdultV-CM is a goal pursued in the ongoing research focused on hiPSC-CM maturation [10].

4.2. I_{CaL} block as an antiarrhythmic therapy

In the present study the effect of blocking I_{CaL} was evaluated through numerous different scenarios. However, a consistent chain of events could be seen in all of them: reduced excitability, increased AP refractoriness, accentuated meandering of the wavefront with a subsequent rise in the wavelength and reduced $f_{reentry}$.

Cellular excitability was studied in a combination of two approaches: the first assessed whether inward currents were mainly responsible for maintaining ventricular re-entry, as had previously been reported for atrial fibrillation [30,31]. The second considered all currents through the SF, since other authors [32–36] had demonstrated that AP propagation/block was due to the source–sink relationship. Moreover, although I_{CaL} and I_{Na} are the principal inward currents, the axial current transmitted by neighbor nodes is critical for cellular depolarization and was not considered in the first approach. Overall, the SF computation was essential to prove not only the reduced cellular excitability, but also the high influence of I_{CaL} and I_{Na} on AP propagation. Both the SF distribution and the normalized map representations yielded extremely similar ZoB, meaning that inward currents are essential for sustained re-entries. These results are in agreement with the above-mentioned findings of Kneller et al. [31] and Liberos et al. [30]. Remarkably, even when I_{Kr} was blocked in-silico to reproduce the effects of verapamil perfusion, the re-entry pattern presented minor variations when compared to the situation in which only I_{CaL} block was modeled. Both single I_{CaL} and combined $I_{CaL} + I_{Kr}$ block yielded similar wavefront meandering and thus almost identical ZoB (see Supporting Information).

Regarding refractoriness, although numerous studies have analyzed the electrophysiological effects of I_{CaL} block in different cardiac tissues this procedure is still controversial. It is well known that the shortening of AP duration (APD) is potentially proarrhythmic since it creates a favorable substrate for arrhythmia maintenance. In this regard, some authors [39] affirm that I_{CaL} block increases the dominant frequency for re-entry since it reduces the APD and refractory period. Others [30,40] however argue that I_{CaL} depression causes $f_{reentry}$ reduction due to the important role of I_{CaL} on AP generation. In the present study we have proved that a considerable block of I_{CaL} (at last of 50%) prolongs refractoriness despite favoring an early repolarization, i. e. althouth blocking I_{CaL} by 50–90% markedly abbreviated the APD, it hampered AP depolarization for high activation rates. Therefore, althouth the APD was shorter, blocking I_{CaL} resulted in a longer effective refractory period (see Suplemental Imporfation – Action potential duration and effective refractory period after I_{CaL} block and Figure S2). In this regard, I_{CaL} block has proved to be crucial in stopping electrical storms in specific cases in which other procedures failed to revert these arrhythmias [41,42], proving its efficacy as a rate-control strategy.

As for wavefront meandering, wavelength and re-entry core size, controversial effects have been reported too. It is commonly accepted that bigger re-entry cores are more likely to induce wavefront collisions and lead to the vanishing of re-entry [30]. In the present work, blocking I_{CaL} increased the meandering of the wavefront in both virtual tissues, with a subsequent increase in the rotor tip movement, re-entry core size and the ZoB. These findings are in agreement with other studies [37,38] which proved that the radius of the re-entry was smaller in control conditions than in a situation characterized by low cellular excitability. In both experimental studies conducted with isolated rabbit hearts and computational simulations done with the Luo-Rudy AP model, re-entry circuits under depressed excitability presented bigger core sizes [37], which implied greater ZoBs. Increased re-entry curvatures were reported after verapamil-induced I_{CaL} block while studying ventricular fibrillation in isolated rabbit hearts [38]. Furthermore, similarly to this study, Samie et al. [37] found that bigger re-entry cores after verapamil administration favored a reduction of the $f_{reentry}$. In the present work smaller $f_{reentry}$ after I_{CaL} block was found in all the scenarios studied, highlighting the agreement between the combined in-vitro/in-silico approach and the hiPSC-CM/hAdultV-CM in-silico comparison.

4.3. Limitations

This work provides an integrated conception of in-vitro and in-silico hiPSC-CM tissues for pharmacological assessment. However, it has several limitations which should be taken into account: first of all, the comparison between hiPSC-CMs and hAdultV-CMs was done in-silico but not in-vitro. Computational models are not perfect descriptions of the cell physiology and do not capture the great complexity of living organisms in their full extent. Moreover, we only compared the effect of I_{CaL} block. Future work should attempt to compare the effects of blocking numerous ionic currents between virtual hiPSC-CMs and hAdultV-CMs in 2D tissues to assess whether the results obtained with hiPSC-CMs can be extrapolated to hAdultV-CMs. Ideally, this comparison should be done both in-silico and in-vitro. Secondly, our in-silico

models do not include accurate anatomical properties of real tissues, such as detailed fiber orientation or electrophysiological heterogeneities. Numerous authors [43,44] have illustrated that the size of the heart, wall thickness and specific fibers distribution determine cardiac function and the characteristics of atrial and ventricular fibrillation. However, our modeling approach considered virtual tissues rather than whole-organ simulations, since we tried to reproduce the tissue patches cultured in-vitro. Moreover, the virtual tissues were modeled with the accurate anisotropic degree and CV of each cell type. Finally, the electrophysiological behavior of both ionic models was analyzed without considering natural variability. Studies [45] analyzing pharmacological outcome in hiPSC-CMs have illustrated how different ionic current distributions might lead to a different response when subject to the same drug. Moreover, hiPSC-CMs are known to present elevated electrophysiological variability [10]. Although this variability was considered in-vitro, the computational models did not include changes in the electrophysiology. In this line, future work should consider a population of virtual tissues developed with a population of hiPSC-CM electrophysiology models.

Despite these limitations, our simulations faithfully reproduce the experimental findings in hiPSC-CMs tissues and shed light on the mechanisms underlying the antiarrhythmic effect of I_{CaL} block. This work also represents an important proof of concept of the reliability of the integration of in-vitro and in-silico experiments using hiPSC-CM tissues for pharmacological assessment.

Disclosures

None.

Sources of funding

This work was supported by the "Plan Estatal de Investigación Científica y Técnica y de Innovación 2017–2020" of the Ministerio de Ciencia e Innovación y Universidades (PID2019-104356RB-C41/AEI/10.13039/501100011033), also by the Dirección General de Política Científica de la Generalitat Valenciana (PROMETEO 2020/043), by the European Union's Horizon 2020 Research and Innovation Programme under Grant Agreement No. 101016496, and by the Agencia Estatal de Investigación [RYC2018-024346-I].

Declaration of competing interest

None declared.

Appendix A. Supplementary data

Supplementary data to this article can be found online at https://doi.org/10.1016/j.compbiomed.2021.104796.

References

[1] N.T. Srinivasan, R.J. Schilling, Sudden cardiac death and arrhythmias, Arrhythmia Electrophysiol. Rev. 7 (2) (2018) 111, https://doi.org/10.15420/aer.2018:15:2.
[2] K. Takahashi, S. Yamanaka, Induction of pluripotent stem cells from mouse embryonic and adult fibroblast cultures by defined factors, Cell 126 (4) (2006) 663–676, https://doi.org/10.1016/j.cell.2006.07.024.
[3] K. Narsinh, K.H. Narsinh, J.C. Wu, Derivation of human induced pluripotent stem cells for cardiovascular disease modeling, Circ. Res. 108 (9) (2011) 1146–1156, https://doi.org/10.1161/circresaha.111.240374.
[4] H. Inoue, S. Yamanaka, The use of induced pluripotent stem cells in drug development, Clinical Pharmacology & Therapeutics 89 (5) (2011) 655–661, https://doi.org/10.1038/clpt.2011.38.
[5] S.M. Wu, K. Hochedlinger, Harnessing the potential of induced pluripotent stem cells for regenerative medicine, Nat. Cell Biol. 13 (5) (2011) 497–505, https://doi.org/10.1038/ncb0511-497.
[6] E. Matsa, D. Rajamohan, E. Dick, L. Young, I. Mellor, A. Staniforth, C. Denning, Drug evaluation in cardiomyocytes derived from human induced pluripotent stem cells carrying a long QT syndrome type 2 mutation, Eur. Heart J. 32 (8) (2011) 952–962, https://doi.org/10.1093/eurheartj/ehr073.
[7] A. Moretti, M. Bellin, A. Welling, C.B. Jung, J.T. Lam, L. Bott-Flügel, K.L. Laugwitz, Patient-specific induced pluripotent stem-cell models for long-QT syndrome, N. Engl. J. Med. 363 (15) (2010) 1397–1409, https://doi.org/10.1056/nejmoa0908679.
[8] P. Liang, K. Sallam, H. Wu, Y. Li, I. Itzhaki, P. Garg, J.C. Wu, Patient-specific and genome-edited induced pluripotent stem cell–derived cardiomyocytes elucidate single-cell phenotype of brugada syndrome, J. Am. Coll. Cardiol. 68 (19) (2016) 2086–2096, https://doi.org/10.1016/j.jacc.2016.07.779.
[9] E. Garreta, L. de Oñate, M.E. Fernández-Santos, R. Oria, C. Tarantino, A. M. Climent, N. Montserrat, Myocardial commitment from human pluripotent stem cells: rapid production of human heart grafts, Biomaterials 98 (2016) 64–78, https://doi.org/10.1016/j.biomaterials.2016.04.003.
[10] M. Paci, K. Penttinen, M. Pekkanen-Mattila, J.T. Koivumäki, Arrhythmia mechanisms in human induced pluripotent stem cell–derived cardiomyocytes, J. Cardiovasc. Pharmacol. 77 (3) (2020) 300–316, https://doi.org/10.1097/fjc.0000000000000972.
[11] C. Tu, B.S. Chao, J.C. Wu, Strategies for improving the maturity of human induced pluripotent stem cell-derived cardiomyocytes, Circ. Res. 123 (5) (2018) 512–514, https://doi.org/10.1161/circresaha.118.313472.
[12] M. Pekkanen-Mattila, M. Häkli, R.-P. Pölönen, T. Mansikkala, A. Junnila, E. Talvitie, K. Aalto-Setälä, Polyethylene terephthalate textiles enhance the structural maturation of human induced pluripotent stem cell-derived cardiomyocytes, Materials 12 (11) (2019) 1805, https://doi.org/10.3390/ma12111805.
[13] T. O'Hara, L. Virág, A. Varró, Y. Rudy, Simulation of the undiseased human cardiac ventricular action potential: model formulation and experimental validation, PLoS Comput. Biol. 7 (5) (2011), e1002061, https://doi.org/10.1371/journal.pcbi.1002061.
[14] M. Paci, J. Hyttinen, B. Rodriguez, S. Severi, Human induced pluripotent stem cell-derived versus adult cardiomyocytes: an in silico electrophysiological study on effects of ionic current block, Br. J. Pharmacol. 172 (21) (2015) 5147–5160, https://doi.org/10.1111/bph.13282.
[15] M. Paci, R.-P. Pölönen, D. Cori, K. Penttinen, K. Aalto-Setälä, S. Severi, J. Hyttinen, Automatic optimization of an in-silico model of human iPSC derived cardiomyocytes recapitulating calcium handling abnormalities, Front. Physiol. 9 (2018), https://doi.org/10.3389/fphys.2018.00709.
[16] D.C. Kernik, S. Morotti, H. Wu, P. Garg, H.J. Duff, J. Kurokawa, C.E. Clancy, A computational model of induced pluripotent stem-cell derived cardiomyocytes incorporating experimental variability from multiple data sources, J. Physiol. 597 (17) (2019) 4533–4564, https://doi.org/10.1113/jp277724.
[17] C.R. Archer, R. Sargeant, J. Basak, J. Pilling, J.R. Barnes, A. Pointon, Characterization and validation of a human 3D cardiac microtissue for the assessment of changes in cardiac pathology, Sci. Rep. 8 (1) (2018), https://doi.org/10.1038/s41598-018-28393-y.
[18] T. Shinozawa, K. Imahashi, H. Sawada, H. Furukawa, K. Takami, Determination of appropriate stage of human-induced pluripotent stem cell–derived cardiomyocytes for drug screening and pharmacological evaluation in vitro, J. Biomol. Screen 17 (9) (2012) 1192–1203, https://doi.org/10.1177/108705711244986.
[19] T. Colatsky, B. Fermini, G. Gintant, J.B. Pierson, P. Sager, Y. Sekino, N. Stockbridge, The comprehensive in vitro proarrhythmia Assay (CiPA) initiative — update on progress, J. Pharmacol. Toxicol. Methods 81 (2016) 15–20, https://doi.org/10.1016/j.vascn.2016.06.002.
[20] Y. Asahi, T. Hamada, A. Hattori, K. Matsuura, M. Odaka, F. Nomura, T. Kaneko, Y. Abe, K. Takasuna, A. Sanbuissho, K. Yasuda, On-chip spatiotemporal electrophysiological analysis of human stem cell derived cardiomyocytes enables quantitative assessment of proarrhythmia in drug development, Sci. Rep. 8 (1) (2018), https://doi.org/10.1038/s41598-018-32921-1.
[21] S. Zlochiver, M. Yamazaki, J. Kalifa, O. Berenfeld, Rotor meandering contributes to irregularity in electrograms during atrial fibrillation, Heart Rhythm 5 (6) (2008) 846–854, https://doi.org/10.1016/j.hrthm.2008.03.010.
[22] M.S. Guillem, A.M. Climent, J. Millet, Á. Arenal, F. Fernández-Avilés, J. Jalife, O. Berenfeld, Noninvasive localization of maximal frequency sites of atrial fibrillation by body surface potential mapping, Circulation: Arrhythmia and Electrophysiology 6 (2) (2013) 294–301, https://doi.org/10.1161/circep.112.000167.
[23] M.T. Mora, J.M. Ferrero, B. Trenor, Ionic Modulation of Calcium Dynamics in Simulated Human Heart Failure. 2017 Computing in Cardiology Conference (CinC). Presented at the 2017 Computing in Cardiology Conference, 2017, https://doi.org/10.22489/cinc.2017.248-074.
[24] P. Taggart, P.M. Sutton, T. Opthof, R. Coronel, R. Trimlett, W. Pugsley, P. Kallis, Inhomogeneous transmural conduction during early ischaemia in patients with coronary artery disease, J. Mol. Cell. Cardiol. 32 (4) (2000) 621–630, https://doi.org/10.1006/jmcc.2000.1105.
[25] E.A. Heidenreich, J.M. Ferrero, M. Doblaré, J.F. Rodríguez, Adaptive macro finite elements for the numerical solution of monodomain equations in cardiac electrophysiology, Ann. Biomed. Eng. 38 (7) (2010) 2331–2345, https://doi.org/10.1007/s10439-010-9997-2.
[26] L. Martinez-Mateu, L. Romero, A. Ferrer-Albero, R. Sebastian, J.F. Rodríguez Matas, J. Jalife, J. Saiz, Factors affecting basket catheter detection of real and phantom rotors in the atria: a computational study, PLoS Comput. Biol. 14 (3) (2018), e1006017, https://doi.org/10.1371/journal.pcbi.1006017.
[27] R.A. Gray, A.M. Pertsov, J. Jalife, Spatial and temporal organization during cardiac fibrillation, Nature 392 (6671) (1998) 75–78, https://doi.org/10.1038/32164.
[28] J.F. Gomez, K. Cardona, L. Romero, J.M. Ferrero, B. Trenor, Electrophysiological and structural remodeling in heart failure modulate arrhythmogenesis. 1D

simulation study, PloS One 9 (9) (2014), e106602, https://doi.org/10.1371/journal.pone.0106602.
[29] M. Lin, H.C. Lucas Jr., G. Shmueli, Research commentary—too big to fail: large samples and thep-value problem, Inf. Syst. Res. 24 (4) (2013) 906–917, https://doi.org/10.1287/isre.2013.0480.
[30] A. Liberos, A. Bueno-Orovio, M. Rodrigo, U. Ravens, I. Hernandez-Romero, F. Fernandez-Aviles, A.M. Climent, Balance between sodium and calcium currents underlying chronic atrial fibrillation termination: an in silico intersubject variability study, Heart Rhythm 13 (12) (2016) 2358–2365, https://doi.org/10.1016/j.hrthm.2016.08.028.
[31] J. Kneller*, J. Kalifa*, R. Zou, A.V. Zaitsev, M. Warren, O. Berenfeld, J. Jalife, Mechanisms of atrial fibrillation termination by pure sodium channel blockade in an ionically-realistic mathematical model, Circ. Res. 96 (5) (2005), https://doi.org/10.1161/01.res.0000160709.49633.2b.
[32] L. Romero, B. Trenor, J.M. Ferrero, C.F. Starmer, Non-uniform dispersion of the source-sink relationship alters wavefront curvature, PloS One 8 (11) (2013), e78328, https://doi.org/10.1371/journal.pone.0078328.
[33] R.M. Shaw, Y. Rudy, Ionic mechanisms of propagation in cardiac tissue, Circ. Res. 81 (5) (1997) 727–741, https://doi.org/10.1161/01.res.81.5.727.
[34] L. Romero, B. Trénor, J.M. Alonso, C. Tobón, J. Saiz, J.M. Ferrero, The relative role of refractoriness and source–sink relationship in reentry generation during simulated acute ischemia, Ann. Biomed. Eng. 37 (8) (2009) 1560–1571, https://doi.org/10.1007/s10439-009-9721-2.
[35] P.M. Boyle, E.J. Vigmond, An intuitive safety factor for cardiac propagation, Biophys. J. 98 (12) (2010) L57–L59, https://doi.org/10.1016/j.bpj.2010.03.018.
[36] P.M. Boyle, W.H. Franceschi, M. Constantin, C. Hawks, T. Desplantez, N. A. Trayanova, E.J. Vigmond, New insights on the cardiac safety factor: unraveling the relationship between conduction velocity and robustness of propagation, J. Mol. Cell. Cardiol. 128 (2019) 117–128, https://doi.org/10.1016/j.yjmcc.2019.01.010.
[37] F.H. Samie, R. Mandapati, R.A. Gray, Y. Watanabe, C. Zuur, J. Beaumont, J. Jalife, A mechanism of transition from ventricular fibrillation to tachycardia, Circ. Res. 86 (6) (2000) 684–691, https://doi.org/10.1161/01.res.86.6.684.
[38] R. Mandapati, Y. Asano, W.T. Baxter, R. Gray, J. Davidenko, J. Jalife, Quantification of effects of global ischemia on dynamics of ventricular fibrillation in isolated rabbit heart, Circulation 98 (16) (1998) 1688–1696, https://doi.org/10.1161/01.cir.98.16.1688.
[39] F.J. Chorro, J. Cánoves, J. Guerrero, L. Mainar, J. Sanchis, L. Such, V. López-Merino, Alteration of ventricular fibrillation by flecainide, verapamil, and sotalol, Circulation 101 (13) (2000) 1606–1615, https://doi.org/10.1161/01.cir.101.13.1606.
[40] Q. Jin, D.J. Dosdall, L. Li, J.M. Rogers, R.E. Ideker, J. Huang, Verapamil reduces incidence of reentry during ventricular fibrillation in pigs, Am. J. Physiol. Heart Circ. Physiol. 307 (9) (2014) H1361–H1369, https://doi.org/10.1152/ajpheart.00256.2014.
[41] D. Erkapic, T. Neumann, J. Schmitt, J. Sperzel, A. Berkowitsch, M. Kuniss, H.-F. Pitschner, Electrical storm in a patient with arrhythmogenic right ventricular cardiomyopathy and SCN5A mutation, Europace 10 (7) (2008) 884–887, https://doi.org/10.1093/europace/eun065.
[42] A. Leenhardt, E. Glaser, M. Burguera, M. Nürnberg, P. Maison-Blanche, P. Coumel, Short-coupled variant of torsade de pointes. A new electrocardiographic entity in the spectrum of idiopathic ventricular tachyarrhythmias, Circulation 89 (1) (1994) 206–215, https://doi.org/10.1161/01.cir.89.1.206.
[43] A. Roy, M. Varela, O. Aslanidi, Image-based computational evaluation of the effects of atrial wall thickness and fibrosis on Re-entrant drivers for atrial fibrillation, Front. Physiol. 9 (2018), https://doi.org/10.3389/fphys.2018.01352.
[44] M. Strocchi, C.M. Augustin, M.A.F. Gsell, E. Karabelas, A. Neic, K. Gillette, O. Razeghi, A.J. Prassl, E.J. Vigmond, J.M. Behar, J. Gould, B. Sidhu, C.A. Rinaldi, M.J. Bishop, G. Plank, S.A. Niederer, A publicly available virtual cohort of four-chamber heart meshes for cardiac electro-mechanics simulations, PloS One 15 (6) (2020), e0235145, https://doi.org/10.1371/journal.pone.0235145.
[45] M. Paci, E. Passini, A. Klimas, S. Severi, J. Hyttinen, B. Rodriguez, E. Entcheva, All-optical electrophysiology refines populations of in silico human iPSC-CMs for drug evaluation, Biophys. J. 118 (10) (2020) 2596–2611, https://doi.org/10.1016/j.bpj.2020.03.018.
[46] J.Q.X. Gong, E.A. Sobie, Population-based mechanistic modeling allows for quantitative predictions of drug responses across cell types, Npj Systems Biology and Applications 4 (1) (2018), https://doi.org/10.1038/s41540-018-0047-2.
[47] A.G. Kléber, Y. Rudy, Basic mechanisms of cardiac impulse propagation and associated arrhythmias, Physiol. Rev. 84 (2) (2004) 431–488, https://doi.org/10.1152/physrev.00025.2003.